Journal of Advanced Research 75 (2025) 331–344

Contents lists available at ScienceDirect

Journal of Advanced Research

journal homepage: www.elsevier.com/locate/jare

Original Manuscript

Asperosaponin VI inhibition of DNMT alleviates GPX4 suppression-mediated osteoblast ferroptosis and diabetic osteoporosis

Fanhao Wei [a,d,1], Binjia Ruan [e,1], Jian Dong [g,1], Bin Yang [b], Guofu Zhang [b], Wai Kwok Kelvin Yeung [h], Hongwei Wang [f,*], Wangsen Cao [b,f,i,*], Yongxiang Wang [b,c,d,e,*]

[a] Department of Graduate School, Dalian Medical University, No.9 of West Section of Lushun South Road, Dalian 116044, China
[b] Department of Orthopaedics, Northern Jiangsu People's Hospital Affiliated to Yangzhou University, 98 West Nantong Road, Yangzhou 225001, China
[c] Department of Orthopaedics, Northern Jiangsu People's Hospital, 98 West Nantong Road, Yangzhou 225001, China
[d] The Yangzhou School of Clinical Medicine of Dalian Medical University, 98 West Nantong Road, Yangzhou 225001, China
[e] Northern Jiangsu People's Hospital, Clinical Teaching Hospital of Medical School, Nanjing University, 98 West Nantong Road, Yangzhou 225001, China
[f] Nanjing University Medical School, Jiangsu Key Lab of Molecular Medicine, 22 Hankou Road, Nanjing 210093, China
[g] Department of Thoracic Surgery, Nanjing Drum Tower Hospital, The Affiliated Hospital of Nanjing University Medical School, Nanjing, Jiangsu 210093, China
[h] Department of Orthopaedics and Traumatology, School of Clinical Medicine, LKS Faculty of Medicine, The University of Hong Kong, Hong Kong, China
[i] Yancheng First People's Hospital, Affiliated Hospital of Nanjing University Medical School, South People's Road, Yancheng 224006, China.

HIGHLIGHTS

- Mouse DOP femurs exhibit GPX4 suppression, ferroptosis, and DNMT1/3a elevation.
- AVI preserves GPX4 and attenuates femoral ferroptotic osteoporosis by inhibiting DNMT1/3a.
- AVI GPX4-sensitively inhibits ferroptotic alterations of osteoblasts.
- Osteoblastic GPX4 deficiency abrogates the antiferroptotic and anti-DOP effects of AVI.
- AVI may be effective in treating DOP and other related osteoporotic disorders.

GRAPHICAL ABSTRACT

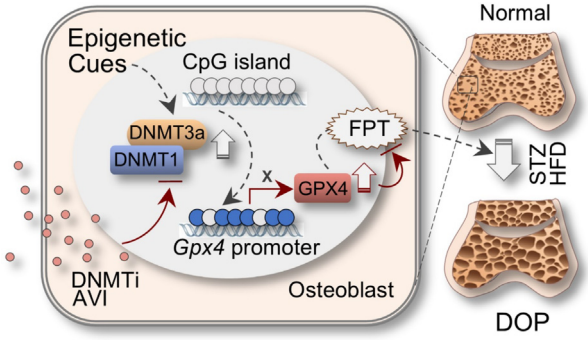

ARTICLE INFO

Article history:
Received 9 July 2024
Revised 21 October 2024
Accepted 29 November 2024
Available online 6 December 2024

Keywords:
Asperosaponin VI
Diabetic Osteoporosis
Ferroptosis
GPX4

ABSTRACT

Introduction: Diabetic osteoporosis (DOP) is an insidious complication of diabetes with limited therapeutic options. DOP is pathologically associated with various types of regulated cell death, but the precise role of ferroptosis in the process remains poorly understood. Asperosaponin VI (AVI), known for its clinical efficacy in treating bone fractures and osteoporosis, may exert its osteoprotective effects through mechanisms involving ferroptosis, however this has not been established.
Objectives: This study aimed to investigate the role of AVI in modulating ferroptosis in a mouse model of DOP and to explore the underlying mechanisms.
Methods: We assessed OP alterations in femurs of DOP-conditioned mice and primary bone cells. We generated a strain of osteoblast-specific *Gpx4*-deficient mice. A combination of micro-CT, immunohistochemistry, immunofluorescence, methylation-specific PCR (MSP), bisulfite sequencing PCR (BSP), western

Abbreviations: DOP, diabetic osteoporosis; AVI, Asperosaponin VI; HFD, high fat diet; GPX4, glutathione Peroxidase 4; BMD, bone mineral density; ALP, Alkaline Posphatase; TRAP, Tartrate-Resistant Acid Phosphatase; HG, high glucose; PA, palmitic acid; DNMT, DNA methyltransferase; BV/TV, bone volume to the total tissue volume; Tb.Th, trabecular thickness; Tb.Sp, trabecular separation; Tb.N, trabecular number; BMM, bone marrow monocytes; TUNEL, terminal deoxynucleotidyl transferase dUTP nick end labeling; H&E, hematoxylin and eosin; HRP, Horseradish peroxidase; IPGTT, intraperitoneal glucose tolerant test; IPITT, Intraperitoneal insulin tolerance test.

* Corresponding authors.
E-mail addresses: hwang@nju.edu.cn (H. Wang), wangsencao@nju.edu.cn (W. Cao), wyx918spine@yzu.edu.cn (Y. Wang).
[1] These authors contributed equally.

https://doi.org/10.1016/j.jare.2024.11.036
2090-1232/© 2024 The Author(s). Published by Elsevier B.V. on behalf of Cairo University.
This is an open access article under the CC BY-NC-ND license (http://creativecommons.org/licenses/by-nc-nd/4.0/).

DNA methylation

blotting (WB), and AVI pull-down assays were employed to elucidate the mechanism and therapeutic target of AVI in DOP.

Results: Our findings revealed that femurs from DOP-conditioned mice exhibited significant ferroptosis and suppression of the core anti-ferroptosis factor GPX4, mainly due to hypermethylation of the *Gpx4* promoter mediated by DNA methyltransferases DNMT1and DNMT3a. Notably, treatment with AVI effectively reversed the hypermethylation, restored GPX4 expression, and reduced ferroptotic pathologies associated with DOP by inhibiting DNMT1/3a. In primarily-cultured osteoblasts and osteoclasts, AVI alleviated GPX4 suppression and reduced ferroptosis in DOP-conditioned osteoblasts through a mechanism dependent on DNMT inhibition and GPX4 restoration. Importantly, the anti-ferroptotic and osteoprotective effects of AVI were abolished in osteoblastic Gpx4 haplo-deficient mice ($Gpx4^{Ob-/+}$) or when GPX4 was pharmacologically inactivated with RSL3.

Conclusions: Our study identifies a pivotal epigenetic ferroptotic pathway that contributes significantly to DOP and uncovers a crucial pharmacological property of AVI that is potentially effective in treating patients with DOP and related osteoporotic disorders.

© 2024 The Author(s). Published by Elsevier B.V. on behalf of Cairo University. This is an open access article under the CC BY-NC-ND license (http://creativecommons.org/licenses/by-nc-nd/4.0/).

Introduction

Diabetic osteoporosis (DOP) is a common complication of diabetes, characterized by reduced bone mass and deteriorated trabecular microarchitecture [1,2]. Due to weaker bone structure and strength, DOP patients face a 20 % higher risk of fragility fracture compared to those without diabetes [3]. While dysregulated glucolipid metabolism is considered the primary etiology of DOP, bone turnover is directly controlled by a dynamic balance between osteoblasts and osteoclasts. Therefore, the activity and fate of these cells are critical for maintaining bone homeostasis [4,5]. Recent studies have highlighted the involvement of the regulated cell death pathways (including apoptosis, necrosis, pyroptosis, ferroptosis, and necroptosis) in the pathogenesis of osteoporosis (OP) [6–9]. However, the precise cellular mechanisms and molecular regulation of ferroptosis in DOP remain partially understood.

Ferroptosis is an iron-dependent form of regulated cell death [10] characterized by lipid peroxidation and mitochondrial dysfunction. It is associated with various pathophysiologies such as tumors, degenerative diseases, ischemia–reperfusion injury and bone diseases [11]. Glutathione peroxidase 4 (GPX4) is a key anti-ferroptotic factor that converts lipid hydroperoxides into non-toxic lipid alcohols [12,13]. GPX4 suppression, whether due to reduced synthesis, protein degradation, or enzyme inactivation, is a hallmark of ferroptosis [14]. Additionally, epigenetic and non-epigenetic regulations of GPX4 transcription influence its expression levels. The *GPX4* promoter contains a dense CpG island, and DNA methylation-induced suppression of GPX4 significantly affects its transcription under various ferroptotic conditions [15]. This suggests that DNA methylation of the *GPX4* promoter may play a critical role in DOP pathogenesis.

In mammals, DNA methylation is catalyzed by DNA methyltransferase DNMT1 (responsible for maintenance methylation), DNMT3a and DNMT3b (responsible for de novo methylation) [16,17]. DNA methylation occurring at CpG islands on the gene promoters and enhancers leads to transcriptional silencing of downstream genes. Conversely, DNA hypomethylation correlates with active gene transcription [18]. Aberrant DNA methylation has been implicated in variety of bone diseases, including osteoarthritis and osteoporosis [19–21]. Synthetic DNMT inhibitors, such as 5-aza-2-deoxycytidine (decitabine), have been approved for the treatment of certain hematopoietic malignancies [22]. However, long-term use of these synthetic epigenetic drugs is associated with adverse side effects (e.g., bleeding and anemia), limiting their use in non-cancerous diseases.

Many natural compounds exhibit strong epigenetic modulation capacities and have a long history of safe clinical use [23,24]. Asperosaponin VI (AVI, PubChem CID:14284436), also known as Akebia Saponin D, is extracted from *Dipsacus asper* [25] and has demonstrated osteogenic activity [26–28]. AVI has been used clinically for many years to treat bone fractures and osteoarthritis with notable efficacy and safety [29]. However, its pharmacological mechanism and molecular targets remain largely unknown. Structurally, AVI is a triterpenoid saponin, and other similar saponins, such as glycyrrhizic acid, have been shown to regulate DNA methylation [30]. This suggests that AVI's osteogeneic effects may involve previously uncharacterized epigenetic regulatory mechanisms.

In this study, we aimed to investigate the mechanism of ferroptosis in a mouse model of DOP. Our findings indicate that GPX4 suppression caused by selective elevation of DNMT1 and DNMT3a and hypermethylation of the *Gpx4* promoter is a critical driver of osteoblast ferroptosis and DOP pathology. Importantly, AVI demonstrated strong DNMT inhibition capacity and effectively reversed GPX4 suppression and ferroptotic changes in DOP mice. Our study brings novel insights into the mechanism of epigenetic ferroptosis involved in DOP and reveals an undiscovered pharmacological property of AVI for its osteoprotective functions with clinical implications.

Materials and methods

Ethics statement

All animal experiments were conducted with approval from the Animal Care Committee of Nanjing University (No. 2020AE01113), following the Institutional Animal Care and Use guidelines.

Animals and model

Male C57BL/6J mice were from Gempharmatech Co., Ltd. (China). To generate osteoblastic *Gpx4* knockout mice, *Gpx4*-flox ($Gpx4^{fl/fl}$; strain No. T050827) mice were crossed with *Col1a1 a1*-Cre (strain no. T004734; GemPharmatech, Nanjing, China) mice. Only heterozygous *Gpx4* deletion progenies *Col1a1-Cre;*$Gpx4^{fl/+}$ ($Gpx4^{Ob-/+}$) were obtained, indicating that homozygous osteoblastic Gpx4 knockout is lethal. PCR genotyping on mouse tail DNAs was performed using primers F1: 5′-GTACTGCAA CAGCTCCG AGTTC, R1: 5′-ACTTATCCAGGCAGACCATGTG, and R2: 5′-AACTCCA ATTCCCAGGACTCAC (Fig. 6A). The experimental mice were housed in ventilated cages (3–5 mice per cage) under a 12-hour light–dark cycles, with daily monitoring of health and regular feed and water replacement.

A DOP mouse model was established as previously described [31]. Four-weeks-old mice were fed a high-fat diet (HFD;

D12492; Research Diet Inc., USA) for 14 weeks, with daily intraperitoneal injections of streptozotocin (STZ, 25 mg/kg, HY-13753, MedChemExpress, USA) starting in week 4 to induce pancreatic β-cell destruction [32]. Six weeks after the HFD began, body weight, blood glucose levels, intraperitoneal glucose tolerant test (IPGTT) and Intraperitoneal insulin tolerance test (IPITT) were assayed to confirm the successful establishment of the model. The study comprised two experimental sets. In the first set, C57BL/6J mice were divided into four groups (n = 6/group): (1) vehicle control; (2) AVI (50 mg/kg, three times per week, intraperitoneal injection, Chengdu Push Biotechnology Co., Ltd., China) or Ferropstatin-1 (Fer-1, 5 mg/kg daily intraperitoneally, HY-100579, MedChemExpress, USA) starting from week 9; (3) DOP model (STZ/HFD); and (4) AVI or Fer-1 as in (2) intervention in DOP mice. The second set of experiment aimed to compare the DOP pathology and the efficacy of AVI intervention between control and RSL3-treated C57BL/6J mice (RSL3, 100 mg/kg, twice a week, intraperitoneally, HY-100218A, MedChemExpress, USA, a GPX4 inactivator) and between $Gpx4^{fl/fl}$ and $Gpx4^{Ob-/+}$ mice. After experiment completion, mouse femurs were surgically collected, fixed in 4 % paraformaldehyde, and stored at − 80 °C for further analysis.

IPGTT and IPITT

IPGTT and IPITT were determined as previously described [31]. Mice were fasted overnight and given an intraperitoneal injection of glucose (2 g/kg, IPGTT) or insulin (0.75 U/kg, CSP001-10, ZQXZ-bio, China, IPITT). Blood specimens were collected from mouse tail and blood glucose was measured at 0, 15, 30, 60, 90, and 120 min using a glucometer (Roche, USA), respectively. Finally, the area under curve (AUC) was calculated from these measurements using the trapezoidal method [33].

Micro-CT analysis

The right femurs of the mice were fixed in 4 % paraformaldehyde for 24 h and scanned using a Scanco μCT80 system (Scanco Medical, Brüttisellen, Switzerland) set at 55 kV, 145 μA, and a voxel size of 15.6 μm with a 250 ms integration time [34]. The three-dimensional (3D) trabecular images were generated from 100 slices per sample. OP parameters, including the ratio of bone volume to total tissue volume (BV/TV), trabecular thickness (Tb.Th), trabecular separation (Tb.Sp), and trabecular number (Tb.N) were calculated.

Primary bone cell culture

Primary osteoblasts were isolated from the calvaria of newborn mice, following an established protocol [35]. Briefly, calvaria were dissected and digested with 0.1 % collagenase A for three rounds, and the final cell preparations were cultured in α-MEM medium containing 10 % fetal bovine serum (FBS). Aalkaline phosphatase (ALP) assays [35] was performed after three passages to confirm osteoblastic identity.

Primary osteoclasts were derived from bone marrow monocytes (BMMs) extracted from the bone marrow of femurs and tibiae of 3-week-old mice [35]. Cells were cultured in α-MEM medium with 10 % FBS and 30 ng/mL macrophage colony-stimulating factor (R&D Systems, USA). After three days, 50 ng/mL of nuclear factor κB receptor activator ligand (RANKL; C28A, Novoprotein, Shanghai, China) was added to induce osteoclast differentiation. verified by tartrate-resistant acid phosphatase (TRAP) staining [35].

A cell model mimicking DOP conditions was established by treating cells with high glucose and palmitic acid (HGPA; HG 25.5 mM and PA 100 μM), with normal glucose (GLU 5.5 mM) serving as control [36,37]. Preliminary tests revealed that after 36 h of HGPA treatment, epigenetic changes in DNMT1/3a and GPX4 expressions, as well as *Gpx4* promoter methylation, resembled those observed in femurs of DOP mice.

Western blotting assay

Western blotting assay was performed on femur homogenates or cultured primary osteoblasts as previously described [34]. Primary antibodies used included GPX4 (A1933, 1:3000) and β-actin (AC026, 1:50000) (ABclonal, China); NFATc1 (AF06823, 1:1000) and DNMT3b (AF300068, 1:1000) from AiFangbiological, China; OPN (GB112328, 1:1000) and Col1a1(GB114197, 1:1000) from Servicebio, China; DNMT1 (ab188453, 1:1000), 4-HNE (ab46545, 1:1000) and TRAP (ab52750, 1:1000) from Abcam, UK; FSP1 (68049–1-Ig, 1:5000) from Proteintech, China; MDA (abx445120, 1:1000) from Abbexa, UK; GAPDH (AF0006, 1:1000); and DNMT3a (AF1732, 1:1000) from Beyotime, China. HRP-conjugated secondary antibodies were from Beyotime, China. Visualization was achieved using the BeyoECL Moon detection system (P0018FS, Beyotime, China) and images were analyzed using ImageJ software, normalized to β-actin/GAPDH, and presented as relative fold changes.

Hematoxylin and eosin, immunohistochemistry, TUNEL, and Perl's Prussian blue staining

Femur sections were processed using hematoxylin and eosin (H&E), immunohistochemistry (IHC), terminal deoxynucleotidyl transferase dUTP nick end labeling (TUNEL), and Perl 's Prussian blue stainings as previously described [34,38]. For IHC, the sections were incubated overnight at 4 °C, with primary antibodies against GPX4 (PA5-109274, 1:100, Thermofisher, USA) and OCN (23418–1-AP, 1:100, proteintech, China). Afterward, the slides were treated with an HRP-conjugated secondary antibody, followed by staining by a DAB HRP Chromogenic Kit (PR30010, Proteintech, China), and counterstained with hematoxylin. TUNEL assays (G1504, Servicebio, China) and Perl's Prussian blue staining (G1029, Servicebio, China) were performed according to the manufacturer's instructions. The stained sections were observed under an Olympus DP74 light microscope or Olympus FV3000 confocal fluorescence microscope. Ten random fields of view per section were selected for quantification, and the mean ratio of positively stained cells was calculated using ImageJ software, applying a double-blind method.

Alkaline phosphatase (ALP) and tartrate-resistant acid phosphatase (TRAP) staining

For ALP activity assay, primary osteoblasts were exposed to high glucose/palmitic acid (HGPA) for 36 h, and then fixed in 4 % formaldehyde for 15 min. The cells were stained using the BCIP/NBT ALP Color Development Kit (P0321, Beyotime, China). Images were captured with an Olympus DP74 light microscope and analyzed using ImageJ software. The area of positive staining at five predetermined positions was calculated and normalized to the total observed area.

For TRAP activity staining, primary osteoclasts exposed to HGPA for 36 h or femoral sections from $Gpx4^{fl/fl}$ and $Gpx4^{Ob-/+}$ mice were stained using a commercial TRAP activity kit (387A-1KT; Sigma, USA), following the manufacturer's instructions. TRAP staining visualizes acid phosphatase activity, producing a burgundy color at the enzyme activity site. Femoral sections were counterstained with methyl green. Images were captured as described above,

and the ratios of positively stained cell areas to total observed areas from 5 predetermined fixed locations were calculated using the ImageJ software via a double-blind method.

Transmission electron microscopy

Ferroptotic changes in mitochondria were examined using transmission electron microscopy. Freshly excised mouse femurs and osteoblasts after various treatments were fixed with electron microscope-grade fixative at 4 °C for 16–24 h. Mitochondrial morphology was observed and photographed using a transmission electron microscope at ShanDong Weiya Biological Technology Co. LTD, China.

Methylation-specific PCR and bisulfite sequencing PCR

CpG islands in the *Gpx4* promoter were predicted and primers for methylation-specific PCR (MSP) and bisulfite sequencing PCR (BSP) were designed using MetPrimer online analyzer (https://www.urogene.org/methprimer). Total DNAs were isolated from femoral tissues or cells using the DNeasy Kit (69504, QIAGEN, Germany), and unmethylated cytosine-to-uracil conversion was performed using the DNA Bisulfite Conversion Kit (DP215, TIANGEN, China). MSP and BSP procedures were performed as previously described [34].

For MSP assays, the following primers were used: methylated forward primer 5′-TTTTTTAAGGGGATGATTTTGATAC (−247/–223, relative to the transcriptional starting site), reverse primer 5′-ATACCCAATAATAAAAA CGCGAA (−78/-100); unmethylated forward primer 5′-TTTTAAGGGGAT GATTTTGATATGT (−245/-221), reverse primer 5′-CATACCCAATAATAA AAACACAAA (−77/-100); input control forward primer 5′-CTCTTTAA GGGGATGACTTTGACAC, reverse primer 5′-ATGCCCAGTGATAGGGA CGCGGG. PCR products were separated by agarose gel electrophoresis, visualized under UV light and analyzed using ImageJ software.

For BSP assay, *Gpx4* promoter-specific primers were used: forward primer 5′- GTTTTTTAAGGGGATGATTTTGATA (−248/-224) and reverse primer 5′- CCCTACAACCAATAAAAAACTAAATA (5/–22). PCR products were separated on agarose gel, purified, and cloned into the pGEM T Easy Vector (A1360; Promega, USA). Five colonies from each PCR reaction were randomly selected for sequencing, and the ratio of methylated cytosines to total cytosines in the cloned fragments was determined.

Reverse-transcription PCR

Total RNA was extracted from mouse femurs using FreeZol reagent (R711-02, Vazyme Biotech, China), and complemental DNA (cDNA) was synthesized using ABSscript Neo RT Master Mix (RK20433, ABclonal, China). Reverse-transcription PCR (RT-PCR) was used to measure *Gpx4* mRNA levels as previously described [34]. Primers used were *Gpx4* forward: 5′-CCCATTCCTGAACCTTTCAA and reverse: 5′-GCACACGAAACCCCTG TACT, *Actb* forward: 5′-GATCATTGCTCCTCCTGAGC and reverse: 5′-TGCACCGCAAGTGCTTCTA serving as the control. PCR products were separated by agarose gel electrophoresis, visualized under ultraviolet light, and analyzed using ImageJ software.

C11-BODIPY

The C11-BODIPY probe (D3861, Thermo Fisher, USA) was used to assess lipid peroxidation in cells, following previously established protocols [39]. After various treatments, osteoblasts were incubated with C11-BODIPY (5 μM) for 30 min. Green and red fluorescence (oxidized BODIPY, excitation/emission 488 nm/510 nm) and red fluorescence (non-oxidized BODIPY, excitation/emission 581 nm/591 nm) were detected using an Olympus FV3000 confocal microscope. Six fields of view were randomly selected for each sample, and e fluorescence intensities were normalized to cell counts and analyzed using ImageJ software.

Plasmid constructions and cell transfection

Two plasmids overexpressing flag-tagged DNMT1 (F-DNMT1) or DNMT3a (F-DNMT3a) were obtained from Corues Biotechnology Co. LTD, China. The plasmids were transfected into primary osteoblasts with Lipofectamine 3000 reagents (Invitrogen, USA) following the manufacturer's instruction. Next day, cells were treated with HGPA and/or AVI and assayed for expression of DNMT1/3a and targeted proteins.

In silico molecular modeling and docking of AVI to DNMT1/3a

Molecular docking simulations of AVI with DNMT1 and DNMT3a were conducted as described previously [40]. The protein structures of DNMT1 (PDB ID: 5WVO) and DNMT3a (PDB ID: 4QBS) were retrieved from the PDB database (https://www.rcsb.org), and AVI structure was obtained from the PubChem (https://pubchem.ncbi.nlm.nih.gov/). Docking simulations were performed using AutoDock (https://autodock.scripps.edu/). Binding affinities (kcal/-mol) were calculated, with lower value indicating more stable binding, and results were analyzed using PyMOL software (https://pymol.org/2/).

Biotinylated-AVI pull-down assay

Biotinylated AVI (bio-AVI) was provided by Xi'an Ruixi Biological Technology Co. LTD, China. A bio-AVI pull-down assay was performed as previously published protocol [41]. Bio-AVI or AVI was incubated with streptavidin-coated beads (P2151; Beyotime, China) for 25 min at room temperature, followed by incubation with primary osteoblast lysates treated with or without HGPA (25.5 mM glucose; 100 μM palmitic acid) at 4 °C for 6 h. Bio-AVI-bound proteins were magnetically separated, washed, resuspended, and analyzed by western blotting to detect DNMT1 and DNMT3a binding.

Statistical analysis

Shapiro-Wilk and Levene's tests were conducted to assess normality and variance for the data. Data were analyzed using GraphPad Prism. Effect sizes (η^2) were calculated using SPSS V22.0, with large effect size defined as $\eta^2 \geq 0.1379$, medium effect size as $0.0588 \leq \eta^2 < 0.1379$, and small effect size as $0.0099 \leq \eta^2 < 0.0588$. Results from animal experiments were presented as mean ± standard error of the mean (SEM), and cell-based results as mean ± standard deviation (SD). Box-and-whisker plots depicted the median (centerline), 25th–75th percentile (box), and minimum/maximum values (whiskers). Group differences were assessed using Student's *t*-test, two-way ANOVA, or two-way ANOVA followed by Tukey's post-hoc test, with statistical significance set at $P < 0.05$.

Results

Mouse DOP femurs exhibit prominent GPX4 suppression and ferroptosis

As the first step in exploring the role of epigenetic ferroptosis in DOP, we established a well-known mouse model of DOP using a combination of HFD feeding and low-dose STZ intraperitoneal injection

(n = 6; Fig. 1A). After 6 weeks, mice showed significant increase in body weight, plasma glucose levels, decreased glucose tolerance and insulin resistance (Fig. 1B and C), indicative of successful model establishment. Micro-CT (μ-CT) and H&E staining revealed significant trabecular degeneration in the distal femurs of DOP mice, including decreased trabecular BV/TV, Tb.N, and Tb.Th, and increased Tb.Sp (Fig. 1D and E). Perl's Prussian blue staining revealed increased iron accumulation, while TUNEL assay detected an increase in positive cells (Fig. 1F). Further examination of bone tissue by western blotting revealed decreased expression of the osteoblast marker Col1a1 and increased expression of the osteoclast marker NFATc1, a typical sign of OP. Notably, there was a decrease in GPX4 expression, a core anti-ferroptosis protein, but not FSP1, another pivotal anti-ferroptosis protein functioning via a GPX4-independent pathway [42]. Down-regulation of GPX4 was accompanied by upregulation of the lipid peroxidation marker 4-HNE (Fig. 1G). IHC staining showed that GPX4 was enriched in control distal femurs, but drastically decreased in DOP mice (Fig. 1H). Transmission electron microscopy (TEM) confirmed broad mitochondrial ferroptotic alterations, such as smaller mitochondria and reduced and diminished mitochondrial crista (Fig. 1I). Furthermore, RT-PCR confirmed that *Gpx4* mRNA level was markedly reduced in the femurs of DOP mice and primary osteoblasts treated with HGPA (Fig. 1J). These results suggest that DOP is associated with significant transcriptional suppression of GPX4 and ferroptosis.

GPX4 suppression is caused by DNTM1/3a elevation and Gpx4 promoter hypermethylation

The mouse *Gpx4* promoter is characterized by conserved CpG Islands stretching from − 210 to 170, relative to the transcriptional starting sites, as analyzed by MetPrime online software (https://www.urogene.org/methprimer) (Fig. 2A). To determine whether aberrant DNA methylation and DNMT expression are involved in DOP, we found that DNMT1 and DNMT3a (but not DNMT3b) were significantly upregulated in DOP-conditioned femurs and primary osteoblasts (Fig. 2B). Treatment with SGI-1027 (a DNMT-selective inhibitor) and AVI restored GPX4 and inhibited 4-HNE and MDA accumulation (Fig. 2C). To ascertain that GPX4 suppression and recovery by AVI involve DNA methylation, we used MSP to analyze the DNA methylation status of the *Gpx4* promoter and found that DOP-conditioned femurs and osteoblasts displayed increased *Gpx4* promoter methylation from 22.36 ± 0.89 % to 65.42 ± 1.26 % ($P < 0.05$) and from 19.85 ± 2.3 % to 69.23 ± 3.91 % ($P < 0.05$; Fig. 2D and E), respectively; however, treatment with SGI-1027 and AVI effectively reduced the levels to 26.51 ± 1.79 % and 25.12 ± 1.78 % ($P < 0.05$) in osteoblasts, whereas AVI reduced the levels to 28.83 ± 0.6 % ($P < 0.05$) in STZ/HFD mice. To confirm these, we performed BSP analysis, the gold standard for the determination of DNA methylation [43]. We randomly picked three mice from each group and cloned and sequenced five BSP products from each mouse. The results showed that CpG methylation in STZ/HFD mice increased from 4.66 ± 0.61 % to 31.12 ± 0.61 % ($P < 0.05$), whereas AVI suppressed it to 14.42 ± 0.6 % ($P < 0.05$; Fig. 2F). Further, overexpression of either flag-tagged DNMT1 or DNMT3a diminished AVI recovery of the GPX4 loss (Fig. 2G). These results suggest that the suppression of GPX4 is primarily due to DNMT aberration-induced *Gpx4* promoter hypermethylation and that AVI reverses GPX4 suppression by inhibiting DNMT1/3a.

AVI inhibits DNMT1/3a probably via promoting their lysosomal degradation

To further elucidate the mechanism by which AVI regulates DNMT1/3a, we performed molecular docking analysis between AVI and the putative targets DNMT1 and DNMT3a [44]. As demonstrated by 3D structure display, AVI was predicted to form hydrogen bonds at ARG74, GLU572, GLN517, GLU514, and SER518 of DNMT1, with a binding energy of −8.8 kcal/mol, and ALA431, GLN428, ARG48, ASN176, ARG45, and ARG44 of DNMT3a, with a binding energy of −11 kcal/mol. These results indicate a strong interaction between AVI and DNMT1/3a proteins (Fig. 3A). We subsequently conducted a pull-down assay by incubating biotinated AVI (bio-AVI, Fig. 3B) with cell lysates of primary osteoblasts and found that DNMT1 and DNMT3a in HGPA-treated cell lysates were pulled down by bio-AVI, indicating a direct interaction between AVI and DNMT1/3a (Fig. 3C). Further, we evaluated the half maximal effective concentrations of AVI (EC50) on DNTM1 and DNMT3a inhibition, which were 4.601 and 5.100 μM, respectively (Fig. 3D and E). A review of the literature revealed that DNMT can be degraded through ubiquitination or autophagy pathway under different conditions [45,46]. To investigate the inhibitory effect of AVI on DNMT1/3a, we treated primary osteoblasts with control, HGPA or AVI/HGPA in absence or presence of MG132 (a ubiquitination inhibitor) or chloroquine (CQ, an autophagy inhibitor), respectively, followed by western blotting. The results showed that CQ, but not MG132, counteracted the inhibitory effects of AVI on DNMT1/3a (Fig. 3F and G). These findings suggest that AVI possesses a potent DNMT inhibitory capacity primarily by promoting lysosomal degradation of DNMT1/3a.

AVI preserves GPX4 and attenuates femoral ferroptotic and osteoporotic pathologies in DOP mice

To further confirm the anti-ferroptosis and osteoprotective effects of AVI *in vivo*, we found that AVI treatment did not alter normal femoral trabecular morphology, but effectively alleviated the trabecular alterations (1.51 ± 0.072 of STZ/HFD vs. 2.24 ± 0.059 of AVI/STZ/HFD, $P < 0.05$), and TUNEL-positive cell counts (28.50 ± 2.217 of STZ/HFD vs. 11.67 ± 1.229 of AVI/STZ/HFD, $P < 0.05$, Fig. 4A and B) in STZ/HFD mice. Notably, Fer-1, a selective inhibitor of ferroptosis [47] also demonstrated similar, although less effective, anti-ferroptotic and osteoprotective effects (Fig. 4A and B, effect size $\eta^2 = 0.487$ of AVI vs. $\eta^2 = 0.472$ of Fer-1). Furthermore, AVI significantly reduced the adverse expression of GPX4, Col1a1, OPN, 4-HNE, NFATc1 and TRAP in STZ/HFD mice (Fig. 4C and D). Overall, these results indicate that AVI inhibits osteo-ferroptosis likely by preserving GPX4, thereby ameliorating OP pathology in DOP mice.

AVI GPX4-sensitively inhibits ferroptotic alterations in osteoblasts

To investigate the cell nature of GPX4 suppression and ferroptosis, we isolated and cultured primary osteoblasts and osteoclasts (differentiated from RANKL-induced bone marrow monocytes/-macrophages), followed by treatment with HGPA. We found that HGPA treatment attenuated ALP activity in osteoblasts and increased TRAP activity in osteoclasts (Fig. 5A and B). Further, we treated these cells with HGPA or the GPX4 inhibitor RSL3 in the absence or presence of AVI. Both HGPA and RSL3 induced increase in TUNEL positive cells in osteoblasts, but not in osteoclasts, while AVI reduced TUNEL-positive cell counts induced by HGPA, but not that by RSL3 (Fig. 5C, the upper two panels). To validate the results, we performed C11-BODIPY staining and found that control osteoblasts overwhelmingly displayed non-oxidized (N-) BODIPY (red), whereas both HGPA and RSL3 caused pronounced increase in oxidized (O-) BODIPY (green) (Fig. 5C, the lower three panels). Furthermore, TEM showed that both HGPA and RSL3 caused ferroptotic mitochondrial changes such as small mitochondria and diminished mitochondria crista. However, AVI effectively corrected these alterations caused by HGPA, but not that by RSL3

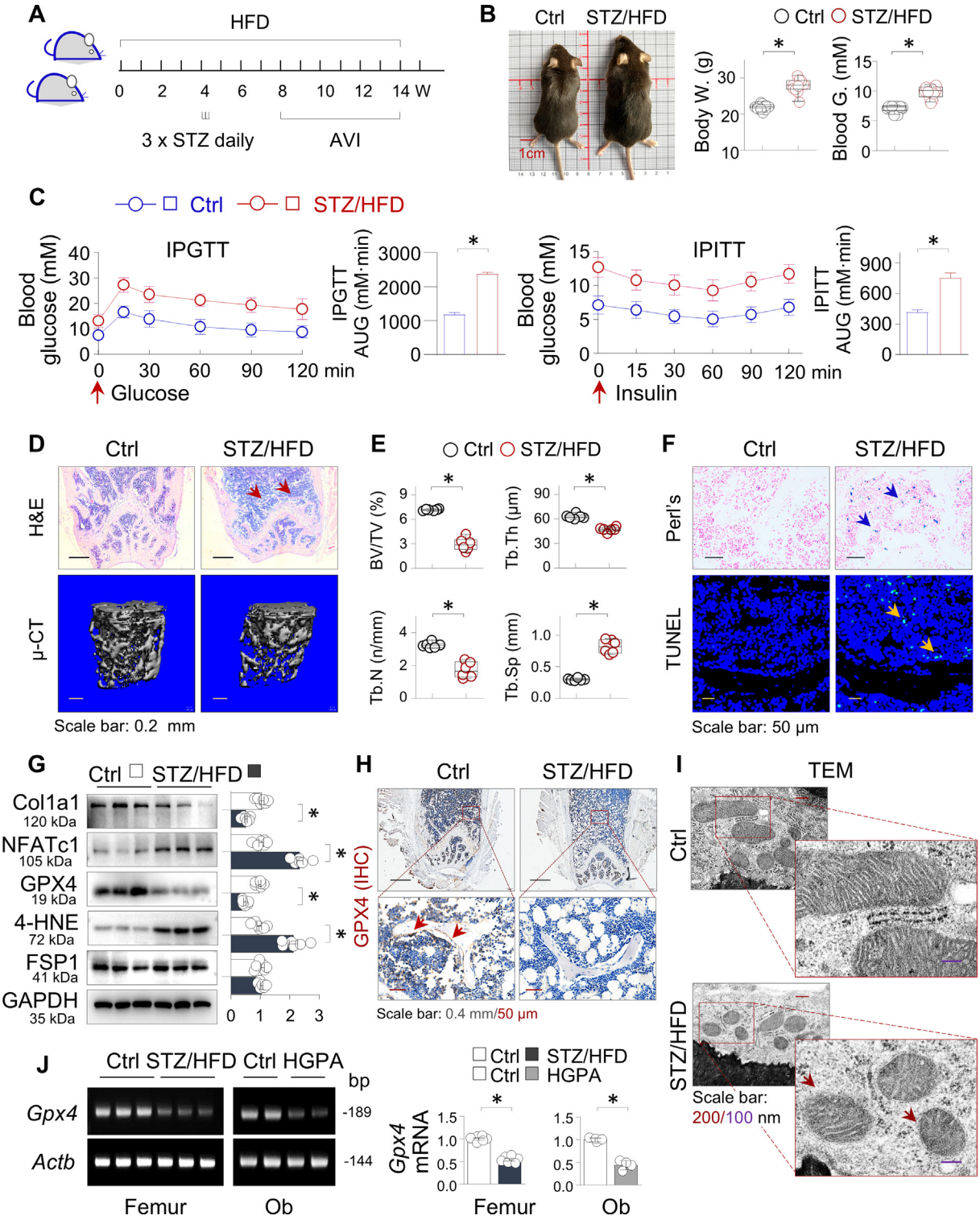

Fig. 1. Mouse DOP femurs exhibit prominent GPX4 suppression and ferroptosis. Four-week-old male C57BL/6J mice were fed an HFD during the experiment (n = 6). After 4 weeks, mice were fasted overnight and then injected daily with STZ (25 mg/kg) intraperitoneally for 3 days to induce type 2 diabetes mellitus. After 8 weeks, mice were given AVI (50 mg/kg) intraperitoneally thrice a week for 6 weeks. **(A)** A schematic illustration of the DOP model established by HFD/STZ treatments. AVI/Fer-1 intervention started from week 9 until completion at weeks 14. **(B)** Gross images of control and STZ/HFD mice, blood glucose and body weight were determined after sixth weeks of HFD feeding. **(C)** Results of IPGTT and IPITT. Time course (0, 15, 30, 60, 90 and 120 min) measurement of blood glucose levels after mice were injected glucose (2 g/kg) for IPGTT or insulin (0.75 U/kg) for IPITT. The area under the curve parameter (AUC) was calculated. Quantification was presented as mean ± SEM. $^{*}P < 0.05$, Student's *t*-test. **(D)** H&E-stained (the upper panel; arrows indicate trabeculae) and μ-CT-scanned (μ-CT, the lower panel) distal femur sections. **(E)** Quantitative analysis of the ratio of bone volume to tissue volume (BV/TV), trabecular number (Tb.N), trabecular thickness (Tb.Th), and trabecular separation (Tb.Sp) of the μ-CT-scanned distal femurs from control (Ctrl) and STZ/HFD mice in Fig. 1D. Box-and-whisker plots, $^{*}P < 0.05$, Student's *t*-test. **(F)** Representative images of distal femur sections stained by Perls' method (the upper panel; arrows indicate iron deposition) and TUNEL (the lower panel; arrows indicate the positively stained cells). **(G)** Western blotting analysis of Col1a1, NFATc1, 4-HNE, FSP1, and GPX4 from mouse femurs (n = 6; three randomly selected samples from each group were shown). GAPDH served as control. Quantification on the right side were presented as mean ± SEM. $^{*}P < 0.05$, Student's *t*-test. **(H)** Representative photomicrographs of distal femur sections stained by immunohistochemistry (IHC) for GPX4 (positively stained cells were indicated by arrows. **(I)** Representative TEM microphotographs. The ferroptotic mitochondria were indicated by arrows. **(J)** RT-PCR. *Gpx4* mRNAs from DOP-conditioned mouse femurs and primary osteoblasts were assessed by RT-PCR and displayed on agarose gel with PCR product sizes displayed in base pairs (bp). *Actb* served as control. Three/two samples from each group were shown. Quantifications on the right side were presented as mean ± SEM, $^{*}P < 0.05$, Student's *t*-test.

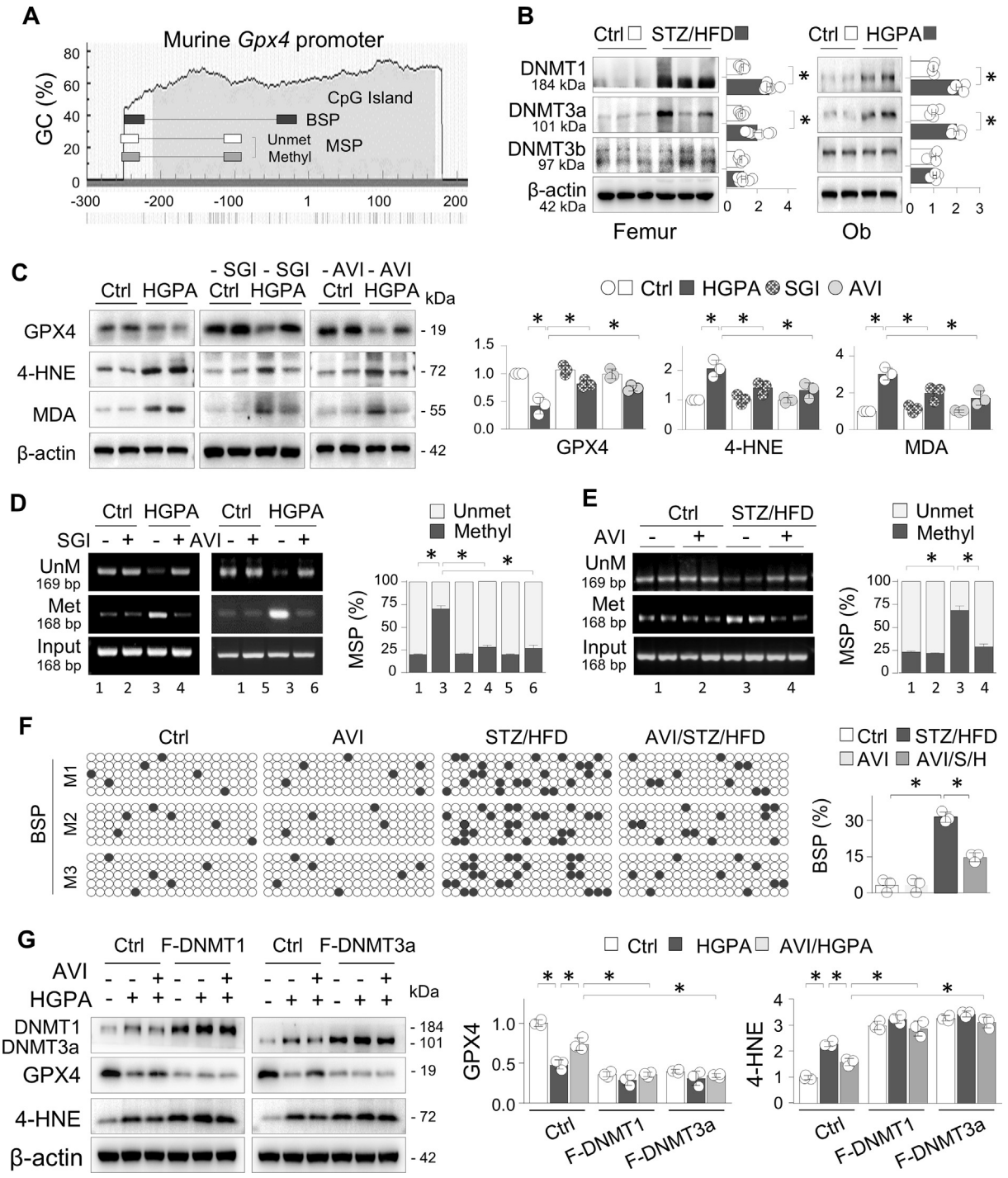

Fig. 2. GPX4 suppression is caused by DNTM1/3a elevation and *Gpx4* promoter hypermethylation. (A) Schematic diagrams of murine *Gpx4* promoter. The positions of CpG islands (gray area) and MSP/BSP primers are depicted relative to the transcription starting site. **(B)** Western blotting of DNMT1, DNMT3a, and DNMT3b from controls and DOP-conditioned mouse femurs and primary osteoblasts (three/two randomly selected samples from each group were shown). β-actin served as control. Quantifications on the right side were presented as mean ± SEM. $^*P < 0.05$, Student's *t*-test. **(C)** Western blotting of GPX4, 4HNE, and MDA from primary osteoblasts treated with HGPA (HG 25.5 mM; PA 100 μM) in presence or absence of Asperosaponin VI (AVI, 10 μM) or SGI-1027(10 μM) for 36 h. Quantifications on the right side were presented as means ± SD. $^*P < 0.05$, one-way ANOVA. **(D)** Representative gel analysis of MSP products from the primary osteoblasts treated as above. Quantification on the right side was presented as mean percentage ± SD after normalized to input PCR products. $^*P < 0.05$, one-way ANOVA. **(E)** Representative gel analysis of MSP products from the experimental mice in Fig. 1A (n = 6, left). Quantification on the right side was presented as mean ± SEM after normalized to input PCR products. $^*P < 0.05$, two-way ANOVA. **(F)** BSP analysis of mouse femurs. For each group, three randomly selected mice (M1, M2, and M3) were analyzed by BSP. Five clones from each animal were sequenced. One box represented one mouse. Each row of dots in the box represents one single sequenced clone, and each dot represents one CpG site. Empty or dark dots indicate unmethylated or methylated CpGs, respectively. Quantification on the right side was presented as mean ratios ± SEM of methylated CpGs over total CpGs in the cloned fragments. $^*P < 0.05$, two-way ANOVA. **(G)** Western blotting. Primary osteoblasts treated with AVI (10 μM) and/or HGPA (HG 25.5 mM; PA 100 μM) in presence or absence of the over-expression of flag-tagged DNMT1 (F-DNMT1) or flag-tagged DNMT3a (F-DNMT3a) for 36 h were assayed for DNMT1, DNMT3a, GPX4 and 4-HNE. β-actin served as control. Quantifications on the right side were presented as mean ± SEM. $^*P < 0.05$, Student's *t*-test.

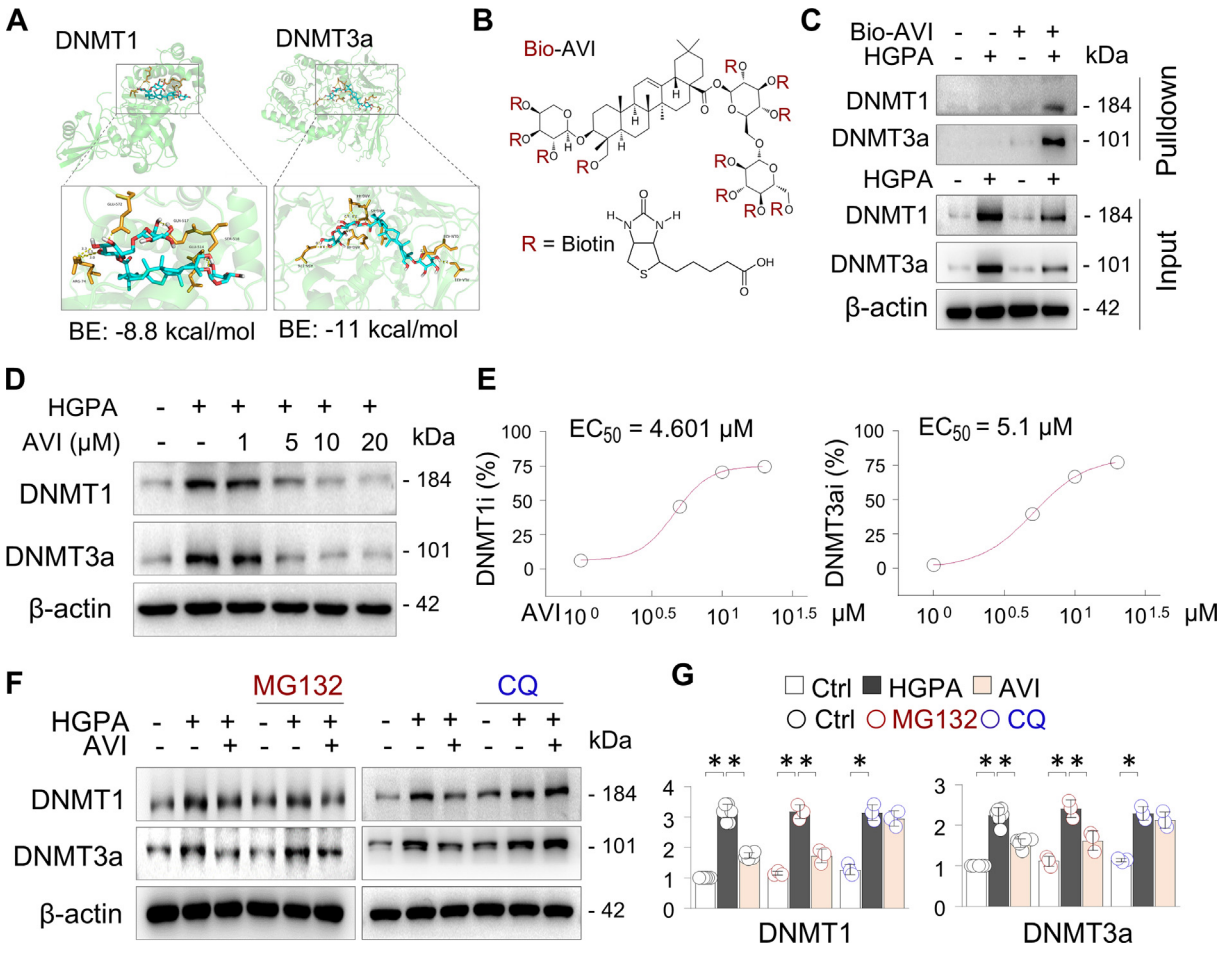

Fig. 3. AVI inhibits DNMT1/3a probably via promoting their lysosomal degradation. **(A)** Molecular docking analysis of AVI binding to DNMT1 and DNMT3a with binding energies of −8.8 and −11 kcal/mol, respectively. **(B)** Structure of Bio-AVI. R = biotin. **(C)** Bio-AVI pull-down assay. Bio-AVI on streptavidin-coated beads was incubated with lysates of primary osteoblasts treated with HGPA (HG 25.5 mM; PA 100 μM) for 6 h. The bound proteins (Pull-down) and total proteins (Input) were assayed for DNMT1 and DNMT3a by western blotting. **(D)** Western blotting. HGPA-treated primary osteoblasts treated with HG/PA (HG 25.5 mM; PA 100 μM) in absence or presence of increasing doses of AVI (1, 5, 10, or 20 μM) for 36 h were assayed for DNMT1 and DNMT3a. **(E)** Quantification of Fig. 3D. Data are presented as mean ± SD of five independent experiments. $^*P < 0.05$, two-way ANOVA. EC50 of DNMT1 and DNMT3a inhibition by AVI are 4.601 and 5.1 μM, respectively. **(F)** Western blotting Primary osteoblasts treated with AVI (10 μM) and/or HGPA (HG 25.5 mM; PA 100 μM) in presence or absence of MG132 (20 μM) or CQ (10 μM) for 36 h were assayed for DNMT1 and DNMT3a. β-actin served as control. **(G)** Quantifications of Fig. 3F. Data were presented as mean ± SD of three repeated experiments, $^*P < 0.05$, two-way ANOVA.

(Fig. 5E). Similarly, AVI effectively alleviated the adverse expression of GPX4, 4HNE, and MDA induced by HGPA, but not that by RSL3 (Fig. 5F and G). Collectively, these results suggest that ferroptosis occurs predominantly in osteoblasts, but not in osteoclasts, under DOP condition and that GPX4 is a crucial mediator of the anti-ferroptosis effects of AVI.

Osteoblast Gpx4 deficiency enhances ferroptotic osteoporosis

To investigate the impact of osteoblast GPX4 suppression on ferroptotic osteoporosis, we intended to generate osteoblast-specific *Gpx4* knockout mice by breeding $Gpx4^{fl/fl}$ mice with *Col1a1-Cre* mice (Fig. 6A). Previous researches have shown that global *Gpx4* knockout is embryonically lethal [48]. In our study, we examined more than 60 offsprings and did not identify homozygous *Gpx4* knockout mice. Instead, live mice were either wild-type or heterozygous *Col1a1-Cre;*$Gpx4^{fl/+}$ ($Gpx4^{Ob-/+}$) (Fig. 6B). This suggests that Gpx4 depletion in osteoblasts is also fatal. At 4 weeks after birth, $Gpx4^{Ob-/+}$ mice were smaller with lighter weights of body and femurs (Fig. 6C), along with reduced femoral GPX4 and decreased OPN and Col1a1 expressions. In contrast, there were no adverse changes in the osteoclast markers NFATc1 and TRAP when compared to control $Gpx4^{fl/fl}$ mice (Fig. 6D). Further, IHC and TRAP staining of femoral sections confirmed reduced OCN, but unchanged TRAP intensity (Fig. 6E). Moreover, these mice exhibited increased TUNEL-positive cell numbers (Fig. 6F), and altered OP parameters: BV/TV, Tb.N, Tb.Th, and Tb.Sp (Fig. 6G), indicating that osteoblast GPX4 haplo-deficiency enhances ferroptosis and osteoporosis.

Osteoblastic GPX4 deficiency abrogates the anti-ferroptotic and osteoprotective effects of AVI in DOP mice

To investigate the critical role of GPX4 preservation by AVI in DOP mice, we compared the anti-ferroptosis and osteoprotective functions of AVI between control and RSL3-treated mice [49,50], as well as between $Gpx4^{fl/fl}$ and $Gpx4^{Ob-/+}$ mice. Both and RSL3-treated and $Gpx4^{Ob-/+}$ mice displayed substantially reduced GPX4 levels and adverse femoral OP alterations of BV/TV, Tb.N and Tb.Sp, along with an increased TUNEL-positive cells (Fig. 7A and B), which were significantly improved after AVI treatment in control and $Gpx4^{fl/fl}$. However, the protective effects were largely abrogated

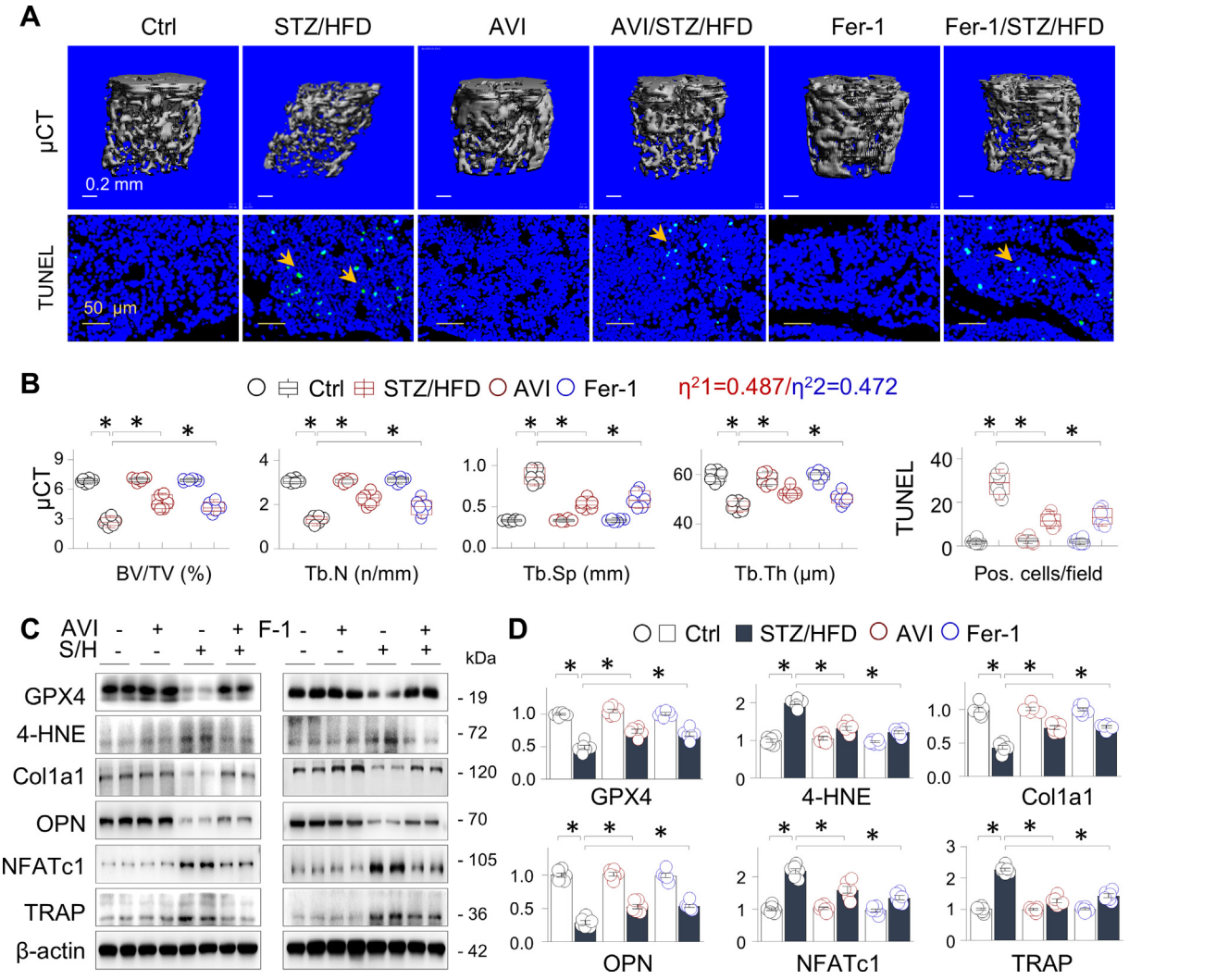

Fig. 4. AVI preserves GPX4 and attenuates femoral ferroptotic and osteoporotic pathologies in DOP mice. C57BL/6J mice were randomly divided into control and STZ/HFD groups. Eight weeks later, these mice were treated with or without AVI (50 mg/kg, thrice a week) or Ferrostatin-1 (Fer-1, 5 mg/kg, daily), respectively, for additional six weeks (n = 6). **(A)** Representative μ-CT-scanned femurs (the upper panel) and TUNEL-stained distal femur sections (the lower panel, arrows indicate the positively-stained cells) of distal femur sections. **(B)** Quantitative analysis of the number of the ratio of bone volume to tissue volume (BV/TV), trabecular number (Tb.N), trabecular thickness (Tb.Th) and trabecular separation (Tb.Sp) of the μ-CT-scanned distal femurs and TUNEL-positive cells in Fig. 4A. Data are presented as box-and-whisker plots. *$P < 0.05$, two-way ANOVA. The effect sizes of interaction between AVI (η1) or ferrostatin-1 (η2) intervention and bone volume fraction are indicated. **(C)** Western blotting assays of GPX4, 4-HNE, Col1a1, OPN, NFATc1, and TRAP of mouse femurs (n = 6, two randomly selected samples are shown). β-actin served as control. **(D)** Quantification of Fig. 4C. Data are presented as mean ± SEM for all tested mouse samples. *$P < 0.05$, two-way ANOVA.

in RSL3-treated and *Gpx4*$^{Ob-/+}$ mice (Fig. 7A and B). Similarly, AVI significantly attenuated the abnormal changes of 4HNE, OPN, Col1a1, TRAP, and NFATc1 in control and *Gpx4*$^{fl/fl}$ mice; but the beneficial effects were largely diminished in RSL3-treated and *Gpx4*$^{Ob-/+}$ mice (Fig. 7C and D). In summary, these results suggest that GPX4 preservation by AVI is crucial for its antiferroptotic and osteoprotective effects.

Discussion

In this study, we have presented key findings that enhance the understanding of the epigenetic mechanisms underlying DOP and the anti-osteoporotic properties of AVI. Our results demonstrated that: (I) STZ/HFD-treated DOP mice exhibited significant suppression of GPX4 and femoral ferroptosis, driven by DNTM1/3a elevation and *Gpx4* promoter hypermethylation; (II) AVI, similar to the DNMT inhibitor (DNMTi) SGI-1027, inhibited DNMT1/3a, likely through promoting their autophagic/lysosomal degradation, and alleviated GPX4 suppression, ferroptosis and DOP pathologies; (III) ferroptosis and GPX4 suppression occurred predominantly in osteoblasts and osteoblast-specific *Gpx4* haplo-defficiency (*Gpx4*$^{Ob-/+}$) led to spontaneous and exacerbated ferroptotic osteoporosis in DOP mice; and (IV) pharmacological inactivation of GPX4 or osteoblast-specific GPX4 haplo-defficiency significantly reduced AVI's osteoprotective effects against DNTM1/3a-mediated ferroptotic DOP pathologies (Fig. 7E). These findings reveal a novel epigenetic mechanism of GPX4 suppression and osteo-ferroptosis in DOP mice, and demonstrated that AVI preserves GPX4 by inhibiting DNMT1/3a, highlighting its potential anti-DOP effects.

An important finding in this study is the identification of GPX4 suppression and osteoblast ferroptosis as a major contributor to DOP. While both osteoblasts and osteoclasts are critically involved in osteoporosis, the death of various bone cells has been shown to be crucial in DOP progression [51,52]. For instance, osteocyte ferroptosis has been reported in diabetic OP and postmenopausal OP modeled by Ovx mice [37,53]. Additionally, osteoclasts are found to mediated bone resorption and ferroptosis that contribute to osteoporosis Our study demonstrated that ferroptosis and GPX4

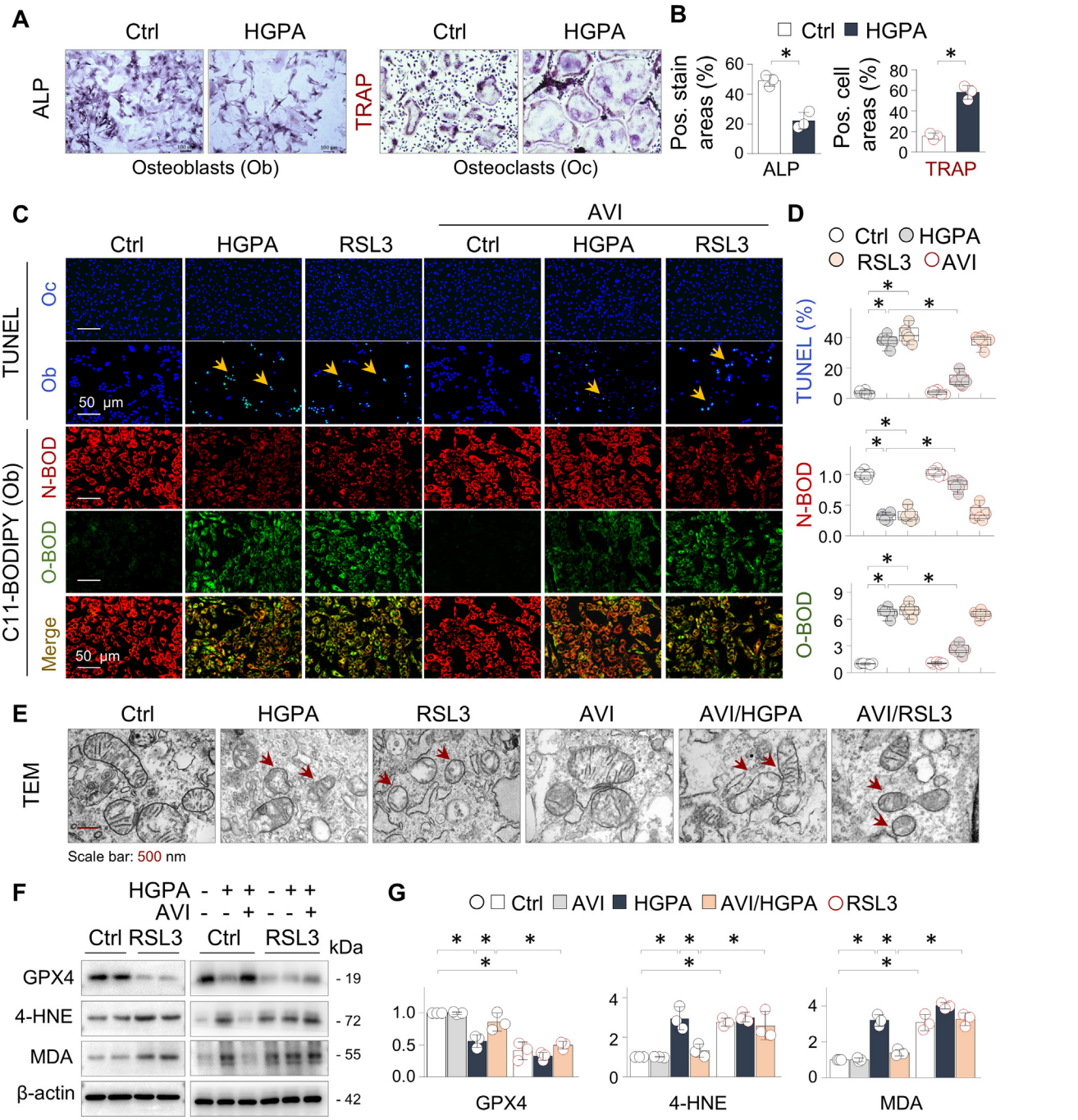

Fig. 5. AVI GPX4-sensitively inhibits HGPA-induced ferroptotic alterations of osteoblasts. (A) Representative images of primary osteoblasts and osteoclasts stained for ALP (alkaline phosphatase, the left panel) and TRAP (tartrate-resistant acid phosphatase, the right panel) activities, respectively. **(B)** Quantification of Fig. 5A was presented as mean ratio of positive staining/cell areas ± SD, n = 3, $^{*}P < 0.05$, Student's *t*-test. **(C)** Representative images of primary osteoblasts and osteoclasts treated with HGPA (HG 25.5 mM; PA 100 μM) or RSL3 (0.3 μM) with or without AVI (10 μM) for 36 h, and then assayed by TUNEL staining (the upper two panels, positively-stained cells were indicated by arrows). Osteoblasts treated as above were examined by C11-BODIPY (the lower three panels). **(D)** Quantifications of TUNEL assays, N-BODIPY, and O-BODIPY of osteoblasts. Data are presented as box-and-whisker plots (n = 4). $^{*}P < 0.05$, two-way ANOVA. **(E)** The osteoblasts treated as above were examined by TEM (arrows indicated ferroptotic mitochondria). **(F)** Western blotting analysis of GPX4, 4-HNE, and MDA of primary osteoblasts treated with RSL3 (0.3 μM), and/or HGPA (HG 25.5 mM; PA 100 μM) in presence or absence of AVI (10 μM) for 36 h. β-actin served as control. **(G)** Quantification of Fig. 5F Data are presented as mean ± SD, n = 3, $^{*}P < 0.05$, two-way ANOVA.

suppression predominantly affected osteoblasts, as evidenced by increased lipid peroxidation, mitochondrial ferroptotic morphology, and osteoblast death, while osteoclasts were unaffected. This was further supported by findings in osteoblast-specific *Gpx4*$^{Ob-/+}$ mice, which exhibited spontaneous and worse ferroptotic osteoporosis compared to STZ/HFD-treated mice. Our results support that osteoblast ferroptosis is a key contributor to DOP pathogenesis.

We found that DNMT1 and DNMT3a are critical initiators of GPX4 suppression, both crucial for the development of osteoporosis in DOP mice. While previous studies have shown that both DOP and ferroptosis are influenced by abnormal DNA methylation [54,55] and that GPX4 suppression due to aberrant DNA methylation plays a vital role in ferroptosis [15,56], the upstream regulators and targets that drive these processes remain incompletely understood. For example, one study showed that local intramedul-

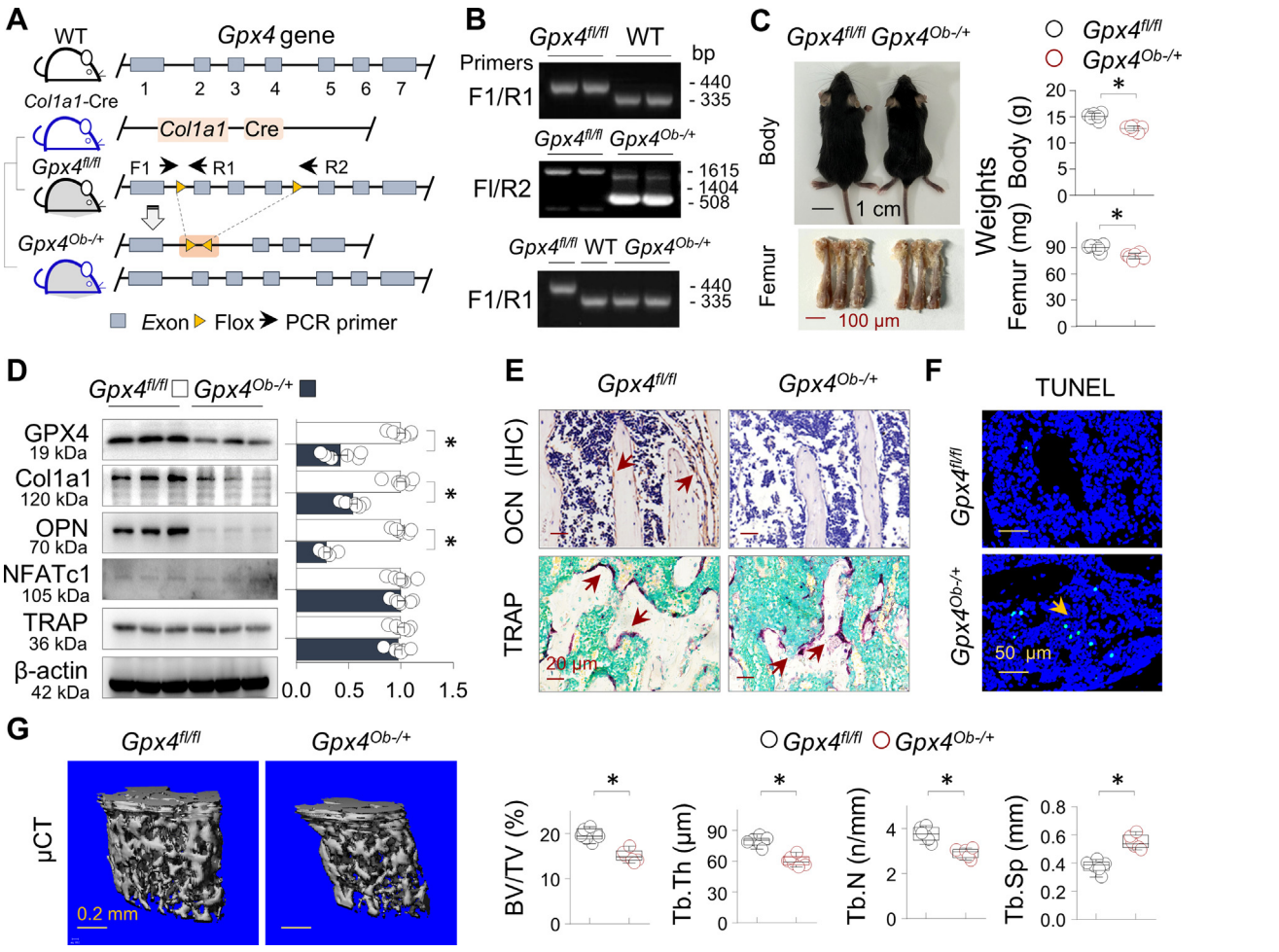

Fig. 6. Osteoblastic GPX4 deficiency potentiates ferroptotic osteoporosis. (A) A diagram of *Gpx4* gene locus in wild-type (WT), *Gpx4*$^{fl/fl}$, and *Gpx4*$^{Ob-/+}$ mice. The *Gpx4* gene contains seven exons represented by boxes. The positions of flox sites (triangles) and genotyping PCR primers F1, R1, and R2 (arrows) are depicted. **(B)** Agarose gel displays of genotyping of WT, *Gpx4*$^{fl/fl}$, and *Gpx4*$^{Ob-/+}$ mice. **(C)** Appearances of (the upper panel) and mouse femurs (the lower panel) of *Gpx4*$^{fl/fl}$ and *Gpx4*$^{Ob-/+}$ mice at 4 weeks. Quantifications of mouse body weight and femur weight were on the right side (n = 6). Data are presented as mean ± SEM. $^*P < 0.05$, Student's *t*-test. **(D)** Western blotting of GPX4, Col1a1, OPN, NFATc1, and TRAP of femoral homogenates from *Gpx4*$^{fl/fl}$ and *Gpx4*$^{Ob-/+}$ mice. Quantifications on the right side were presented as mean ± SEM. $^*P < 0.05$, Student's *t*-test. **(E)** Representative IHC images of femur sections from *Gpx4*$^{fl/fl}$ and *Gpx4*$^{Ob-/+}$ mice stained for OCN and TRAP. The arrows indicated the positively-stained signals. **(F)** Representative TUNEL-stained distal femoral sections of *Gpx4*$^{fl/fl}$ and *Gpx4*$^{Ob-/+}$ mice. Arrows indicated positively-stained cells. **(G)** Representative microphotographs of μ-CT-scanned distal femurs of *Gpx4*$^{fl/fl}$ and *Gpx4*$^{Ob-/+}$ mice. Quantitative analysis of μ-CT 3D reconstruction data in Fig. 6G. was on the right side for the ratio of bone volume to tissue volume (BV/TV), trabecular number (Tb.N), trabecular thickness (Tb.Th), and trabecular separation (Tb.Sp). Data are presented as box-and-whisker plots. $^*P < 0.05$, n = 6, Student's *t*-test.

lary injection of DNMT1 siRNA restored femoral microstructure in a rat model of disuse OP [57]. Another study demonstrated that running exercise inhibited DNMT1/3a/3b elevation and reversed Nrf2 promoter hypermethylation, alleviating osteoporosis in ovariectomized mice [34]. We observed that GPX4 suppression in DOP was linked to DNMT1/3a elevation and hypermethylation of the *Gpx4* promoter. We further demonstrated that treatment with the DNMT inhibitor SGI-1027 effectively reversed GPX4 suppression and ameliorated osteoblast ferroptosis, which were significantly blocked by DNMT1/3a overexpression. Therefore, our study identified DNMT1 and DNMT3a as the key upstream regulators of GPX4 suppression-associated osteoblast ferroptosis critically involved in DOP pathogenesis, underscoring an effective and targeted strategy to treat DOP.

Many compounds in herbal medicines, such as polyphenols, flavonoids, and alkaloids, exhibit strong DNA methylation-regulatory properties [58]. For instance, glycyrrhizic acid, a saponin structurally similar to AVI, has been shown to inhibit DNMT1/3a and exert antifibrotic effects in lung fibrosis mice [30]. However, the mechanisms behind AVI's osteogenic effects in DOP remain unclear. Our study found that AVI inhibits the abnormal elevation of DNMT1/3a in DOP mice and osteoblasts. Molecular modeling and bio-AVI pull-down assay confirmed AVI's strong binding to DNMT1 and DNMT3a, making them key targets for AVI's demethylating action. Furthermore, AVI showed prominent osteogenic efficacy compared to synthetic DNMT inhibitor SGI-1027, and inhibited DNMT1 (EC50 8.203 μM) and DNMT3a (EC50 7.725 μM) likely via lysosomal degradation, with higher electivity for DNMT3a. These findings position AVI as an effective epigenetic DNMT inhibitor and may explain many of its osteogenic or other tissue-protective functions.

Conclusion

Our results show that AVI inhibits osteoblast ferroptosis and alleviates bone loss in DOP mice by inhibiting the aberrant elevation of DNMT1/3a and *Gpx4* promoter hypermethylation. These findings uncover a unique epigenetic mechanism of ferroptosis

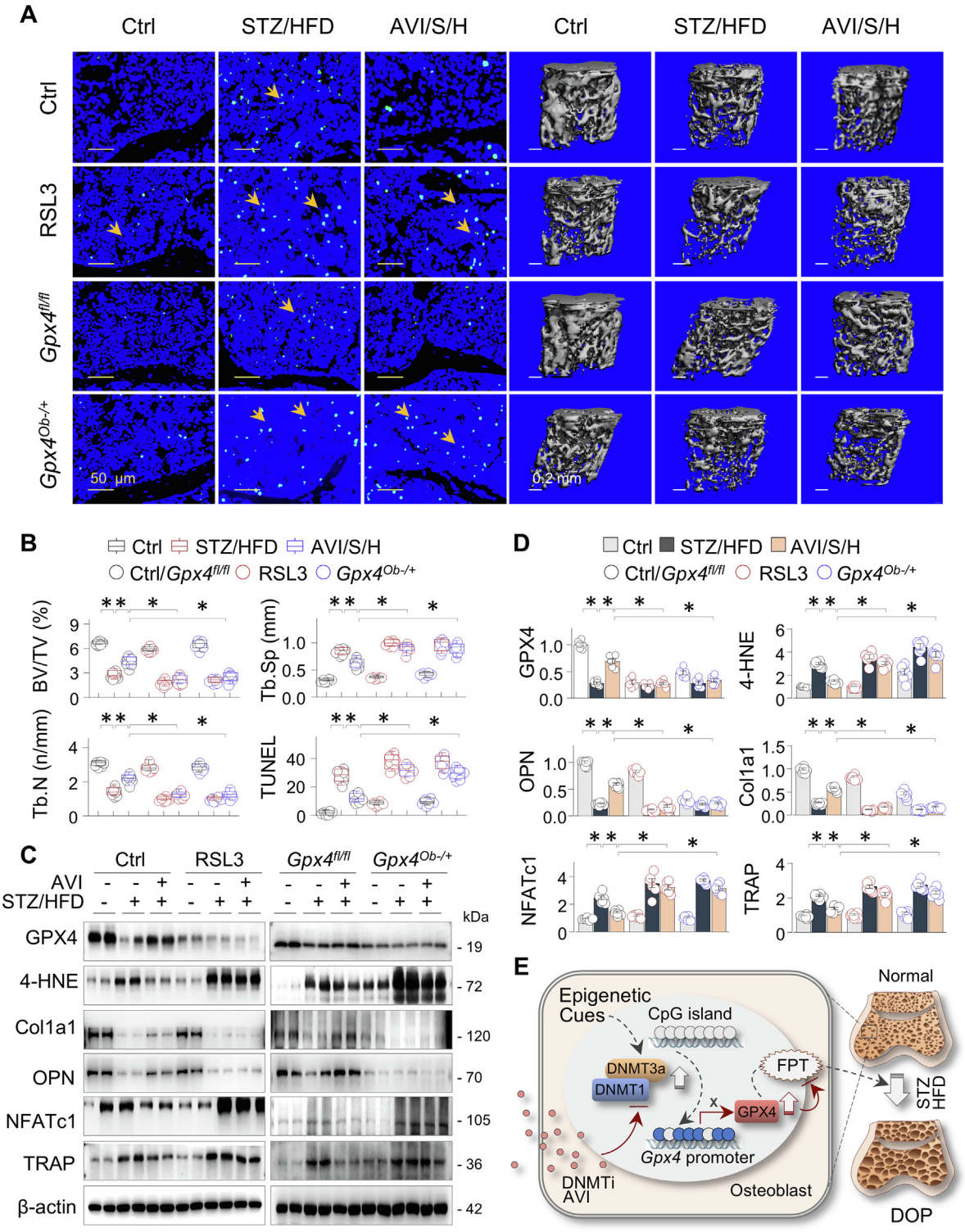

Fig. 7. Osteoblastic GPX4 deficiency attenuates the anti-ferroptotic and osteoprotective effects of AVI in DOP mice. Control (Ctrl) and RSL3-treated mice, as well as *Gpx4*$^{fl/fl}$ and *Gpx4*$^{Ob-/+}$ mice, were subjected to vehicle control (Ctrl), STZ/HFD, or AVI/ STZ/HFD treatment as before (n = 6). **(A)** Representative microphotographs of the μ-CT-scanned distal femurs (the left panel) and TUNEL-stained femur sections (the right panel, Arrows indicated the positive cells). **(B)** Quantitative analysis of the ratio of bone volume to tissue volume (BV/TV), trabecular number (Tb.N), trabecular separation (Tb.Sp), and TUNEL staining in Fig. 7A. Data are presented as box-and-whisker plots. $^{*}P < 0.05$, two-way ANOVA with Tukey's post-hoc test. **(C)** Western blotting of GPX4, 4-HNE, Col1a1, OPN, NFATc1, and TRAP of femoral homogenates from the mice in Fig. 7A (n = 6, two samples from each group were shown). β-actin served as control. **(D)** Quantification of Fig. 7C Data were presented as mean ± SEM. $^{*}P < 0.05$, Two-way ANOVA. **(E)** A schematic diagram depicting sequential DNMT1/3a elevation, hypermethylation of the *Gpx4* promoter, GPX4 transcription inhibition, osteoblast ferroptosis (FPT) and DOP in STZ/HFD mice. Conversely, DNMT inhibition (DNMTi)/AVI reverse the process by inhibiting DNMT1/3a.

involved in DOP, and highlight a novel aspect of AVI's pharmacology for its therapeutic potential to treat DOP and other related osteoporotic disorders.

Compliance with ethics requirements

All Institutional and National Guidelines for the care and use of animals (fisheries) were followed.

The use of animals and the experimental protocols were approved by the Animal Care Committee of Nanjing University (No. 2020AE01113) in accordance with the Institutional Animal Care and Use guidelines.

CRediT authorship contribution statement

Fanhao Wei: Methodology, Investigation, Data curation, Formal analysis, Software, Visualization, Validation, Writing – original draft, Writing – review & editing. **Binjia Ruan:** Methodology, Investigation, Data curation, Formal analysis, Software, Visualization, Writing – original draft. **Jian Dong:** Methodology, Investigation, Formal analysis, Data curation, Software, Visualization, Validation, Writing – original draft. **Bin Yang:** Formal analysis, Investigation. **Guofu Zhang:** Investigation, Validation. **Wai Kwok Kelvin Yeung:** Investigation, Visualization. **Hongwei Wang:** Data curation, Formal analysis, Supervision, Validation, Resources. **Wangsen Cao:** Conceptualization, Methodology, Data curation, Formal analysis, Writing – original draft, Writing – review & editing, Visualization, Supervision, Validation, Resources, Funding acquisition. **Yongxiang Wang:** Methodology, Resources, Data curation, Formal analysis, Supervision, Funding acquisition. All authors approved the final version of the manuscript

Declaration of competing interest

The authors declare that they have no known competing financial interests or personal relationships that could have appeared to influence the work reported in this paper.

Acknowledgment

This work was supported by the National Key Research and Development Program of China (2023YFB3810200, 2023YFB3810204), the National Natural Science Foundation of China (82470749, 82272502, 82072423), the Jiangsu Province Traditional Chinese medicine science and technology development program (ZT202117), Jiangsu Province "333 project" key industry talents (BRA202201) and Yangzhou key research and development plan (social development) project (YZ2022070). the China Medical Education Association 2022 major scientific problems and key topics of medical technology problems (2022KTM022) and the Postgraduate Research & Practice Innovation Program of Jiangsu Province (KYCX21_3288).

References

[1] Paschou SA et al. Type 2 diabetes and osteoporosis: a guide to optimal management. J Clin Endocrinol Metab 2017;102(10):3621–34.
[2] de Araujo IM, Moreira MLM, de Paula FJA. Diabetes and bone. Arch Endocrinol Metab 2022;66(5):633–41.
[3] Dede AD et al. Type 2 diabetes mellitus and fracture risk. Metabolism 2014;63(12):1480–90.
[4] Wang Z et al. Autophagy mediated CoCrMo particle-induced peri-implant osteolysis by promoting osteoblast apoptosis. Autophagy 2016;11(12):2358–69.
[5] Pellegrini G et al. Avenanthramides Prevent Osteoblast and Osteocyte Apoptosis and Induce Osteoclast Apoptosis in Vitro in an Nrf2-Independent Manner. Nutrients 2016;8(7):423.
[6] Li Z et al. Cell death regulation: A new way for natural products to treat osteoporosis. Pharmacol Res 2023;187:106635.
[7] Wang J et al. The role of autophagy in bone metabolism and clinical significance. Autophagy 2023;19(9):2409–27.
[8] Gao L et al. Molecular mechanism of ferroptosis in orthopedic diseases. Cells 2022;11(19).
[9] Xu C-Y et al. Poliumoside protects against type 2 diabetes-related osteoporosis by suppressing ferroptosis via activation of the Nrf2/GPX4 pathway. Phytomedicine 2024;125:155342.
[10] Xie L, Fang B, Zhang C. The role of ferroptosis in metabolic diseases. Biochim Biophys Acta Mol Cell Res 2023;1870(6):119480.
[11] Jiang X, Stockwell BR, Conrad M. Ferroptosis: mechanisms, biology and role in disease. Nat Rev Mol Cell Biol 2021;22(4):266–82.
[12] Liu Y et al. GPX4: The hub of lipid oxidation, ferroptosis, disease and treatment. Biochim Biophys Acta Rev Cancer 2023;1878(3):188890.
[13] Stoyanovsky DA et al. Iron catalysis of lipid peroxidation in ferroptosis: regulated enzymatic or random free radical reaction? Free Radic Biol Med 2019;133:153–61.
[14] Stockwell BR et al. Ferroptosis: a regulated cell death nexus linking metabolism, redox biology, and disease. Cell 2017;171(2):273–85.
[15] Zhang X et al. Homocysteine induces oxidative stress and ferroptosis of nucleus pulposus via enhancing methylation of GPX4. Free Radic Biol Med 2020;160:552–65.
[16] Chen Z, Zhang Y. Role of mammalian DNA methyltransferases in development. Annu Rev Biochem 2020;89:135–58.
[17] Del Castillo Falconi VM et al. DNA methyltransferases: from evolution to clinical applications. Int J Mol Sci 2022;23(16).
[18] Wu C et al. Interplay of m6A and H3K27 trimethylation restrains inflammation during bacterial infection. Sci Adv 2020;6(34):eaba0647.
[19] Peng S et al. JKAMP inhibits the osteogenic capacity of adipose-derived stem cells in diabetic osteoporosis by modulating the Wnt signaling pathway through intragenic DNA methylation. Stem Cell Res Ther 2021;12(1):120.
[20] Sarkar A et al. STAT3 promotes a youthful epigenetic state in articular chondrocytes. Aging Cell 2023;22(2):e13773.
[21] Takahashi A et al. DNA methylation of the RUNX2 P1 promoter mediates MMP13 transcription in chondrocytes. Sci Rep 2017;7(1):7771.
[22] Tsai H-C et al. Transient low doses of DNA-demethylating agents exert durable antitumor effects on hematological and epithelial tumor cells. Cancer Cell 2012;21(3):430–46.
[23] Zhang G et al. Therapeutic approach of natural products that treat osteoporosis by targeting epigenetic modulation. Front Genet 2023;14.
[24] Guo W et al. Epigenetic studies of Chinese herbal medicine: pleiotropic role of DNA methylation. Front Pharmacol 2021;12.
[25] Zhou Y-Q et al. Akebia saponin D, a saponin component from Dipsacus asper Wall, protects PC 12 cells against amyloid-beta induced cytotoxicity. Cell Biol Int 2009;33(10):1102–10.
[26] Ke K et al. Asperosaponin VI promotes bone marrow stromal cell osteogenic differentiation through the PI3K/AKT signaling pathway in an osteoporosis model. Sci Rep 2016;6:35233.
[27] Niu Y et al. Asperosaponin VI, a saponin component from Dipsacus asper wall, induces osteoblast differentiation through bone morphogenetic protein-2/p38 and extracellular signal-regulated kinase 1/2 pathway. Phytother Res : PTR 2011;25(11):1700–6.
[28] Chen F et al. Synergy effects of Asperosaponin VI and bioactive factor BMP-2 on osteogenesis and anti-osteoclastogenesis. Bioact Mater 2022;10:335–44.
[29] Gu M et al. Akebia Saponin D suppresses inflammation in chondrocytes via the NRF2/HO-1/NF-κB axis and ameliorates osteoarthritis in mice. Food Funct 2020;11(12):10852–63.
[30] Wei A et al. Inhibition of DNA methylation de-represses peroxisome proliferator-activated receptor-γ and attenuates pulmonary fibrosis. Br J Pharmacol 2022;179(7):1304–18.
[31] Zhang C et al. Nuciferine ameliorates hepatic steatosis in high-fat diet/streptozocin-induced diabetic mice through a PPARα/PPARγ coactivator-1α pathway. Br J Pharmacol 2018;175(22):4218–28.
[32] Nath S, Ghosh SK, Choudhury Y. A murine model of type 2 diabetes mellitus developed using a combination of high fat diet and multiple low doses of streptozotocin treatment mimics the metabolic characteristics of type 2 diabetes mellitus in humans. J Pharmacol Toxicol Methods 2017;84:20–30.
[33] Fukumura K et al. Effects of overexpression of neurosecretory protein GL-precursor gene on glucose homeostasis and insulin sensitivity in mice. Int J Mol Sci 2021;22(9).
[34] Chen X et al. Nrf2 epigenetic derepression induced by running exercise protects against osteoporosis. Bone Res 2021;9(1):15.
[35] Dong, J., et al., *NRF2 is a critical regulator and therapeutic target of metal implant particle-incurred bone damage.* Biomaterials, 2022. **Online ahead publication**: p. 121742.
[36] Lin Y et al. Activation of osteoblast ferroptosis via the METTL3/ASK1-p38 signaling pathway in high glucose and high fat (HGHF)-induced diabetic bone loss. FASEB J 2022;36(3):e22147.
[37] Yang Y et al. Targeting ferroptosis suppresses osteocyte glucolipotoxicity and alleviates diabetic osteoporosis. Bone Res 2022;10(1):26.
[38] Zhang L et al. HDAC3 aberration-incurred GPX4 suppression drives renal ferroptosis and AKI-CKD progression. Redox Biol 2023;68:102939.
[39] Drummen GPC et al. C11-BODIPY(581/591), an oxidation-sensitive fluorescent lipid peroxidation probe: (micro)spectroscopic characterization and validation of methodology. Free Radic Biol Med 2002;33(4):473–90.

[40] Seeliger D, de Groot BL. Ligand docking and binding site analysis with PyMOL and Autodock/Vina. J Comput Aided Mol Des 2010;24(5):417–22.
[41] Xu H et al. Costunolide covalently targets NACHT domain of NLRP3 to inhibit inflammasome activation and alleviate NLRP3-driven inflammatory diseases. Acta Pharm Sin B 2023;13(2):678–93.
[42] Bersuker K et al. The CoQ oxidoreductase FSP1 acts parallel to GPX4 to inhibit ferroptosis. Nature 2019;575(7784):688–92.
[43] Zhou Y et al. DNMT3A facilitates colorectal cancer progression via regulating DAB2IP mediated MEK/ERK activation.. Biochim Biophys Acta Mol Basis Disease 2022;1868(4):166353.
[44] Pinzi L, Rastelli G. Molecular docking: shifting paradigms in drug discovery. Int J Mol Sci 2019;20(18).
[45] Du Z et al. DNMT1 stability is regulated by proteins coordinating deubiquitination and acetylation-driven ubiquitination. Sci Signal 2010;3 (146):ra80.
[46] Zhang X et al. TXNIP, a novel key factor to cause Schwann cell dysfunction in diabetic peripheral neuropathy, under the regulation of PI3K/Akt pathway inhibition-induced DNMT1 and DNMT3a overexpression. Cell Death Dis 2021;12(7):642.
[47] Dixon SJ et al. Ferroptosis: an iron-dependent form of nonapoptotic cell death. Cell 2012;149(5):1060–72.
[48] Yoo S-E et al. Gpx4 ablation in adult mice results in a lethal phenotype accompanied by neuronal loss in brain. Free Radic Biol Med 2012;52 (9):1820–7.
[49] Sun X et al. TRIM21 ubiquitylates GPX4 and promotes ferroptosis to aggravate ischemia/reperfusion-induced acute kidney injury. Life Sci 2023;321:121608.
[50] Lin Z et al. *Hypoxia-induced HIF-1α/lncRNA-PMAN inhibits ferroptosis by promoting the cytoplasmic translocation of ELAVL1 in peritoneal dissemination from gastric cancer*. Redox Biology 2022;52:102312.
[51] McHugh J. Osteocyte death promotes bone loss. Nat Rev Rheumatol 2020;16 (10):539.
[52] Andreev D et al. Osteocyte necrosis triggers osteoclast-mediated bone loss through macrophage-inducible C-type lectin. J Clin Invest 2020;130 (9):4811–30.
[53] Jiang, Z., et al., *Ferroptosis in Osteocytes as a Target for Protection Against Postmenopausal Osteoporosis.* Advanced Science (Weinheim, Baden-Wurttemberg, Germany), 2024. **11**(12): p. e2307388.
[54] Wang X et al. Effects of DNA, RNA, and protein methylation on the regulation of ferroptosis. Int J Biol Sci 2023;19(11):3558–75.
[55] Letarouilly JG, Broux O, Clabaut A. New insights into the epigenetics of osteoporosis. Genomics 2019;111(4):793–8.
[56] Shang J et al. Gossypol acetic acid alleviates the ferroptosis of chondrocytes in osteoarthritis by inhibiting GPX4 methylation. Curr Med Chem 2024.
[57] Li B et al. Overexpression of DNMT1 leads to hypermethylation of H19 promoter and inhibition of Erk signaling pathway in disuse osteoporosis. Bone 2018;111:82–91.
[58] Huang Z et al. Epigenetic regulation of active Chinese herbal components for cancer prevention and treatment: A follow-up review. Pharmacol Res 2016;114.